Tuning the Coordination Structure of Cu–N–C Single Atom Catalysts for Simultaneous Electrochemical Reduction of CO_2 and NO_3^- to Urea

Josh Leverett, Thanh Tran-Phu, Jodie A. Yuwono, Priyank Kumar, Changmin Kim, Qingfeng Zhai, Chen Han, Jiangtao Qu, Julie Cairney, Alexandr N. Simonov, Rosalie K. Hocking, Liming Dai, Rahman Daiyan,* and Rose Amal**

Closing both the carbon and nitrogen loops is a critical venture to support the establishment of the circular, net-zero carbon economy. Although single atom catalysts (SACs) have gained interest for the electrochemical reduction reactions of both carbon dioxide (CO_2RR) and nitrate (NO_3RR), the structure–activity relationship for Cu SAC coordination for these reactions remains unclear and should be explored such that a fundamental understanding is developed. To this end, the role of the Cu coordination structure is investigated in dictating the activity and selectivity for the CO_2RR and NO_3RR. In agreement with the density functional theory calculations, it is revealed that Cu-N_4 sites exhibit higher intrinsic activity toward the CO_2RR, whilst both Cu-N_4 and Cu-N_{4-x}-C_x sites are active toward the NO_3RR. Leveraging these findings, CO_2RR and NO_3RR are coupled for the formation of urea on Cu SACs, revealing the importance of *COOH binding as a critical parameter determining the catalytic activity for urea production. To the best of the authors' knowledge, this is the first report employing SACs for electrochemical urea synthesis from CO_2RR and NO_3RR, which achieves a Faradaic efficiency of 28% for urea production with a current density of –27 mA cm^{-2} at –0.9 V versus the reversible hydrogen electrode.

1. Introduction

Electrochemical approaches to closing both the carbon and nitrogen cycles have emerged as promising routes toward decarbonization of the world economy and a shift toward energy sustainability and enabling a circular economy. The electrochemical carbon dioxide reduction reaction (CO_2RR) powered with renewable electricity provides a pathway for simultaneously alleviating the emissions of waste CO_2 to the atmosphere, whilst converting intermittent renewable energy to value-added and stable chemical commodities (through a renewable Power-to-X platform).[1] For example, one such product of CO_2RR gaining recent interest is synthesis gas (or syngas), a mixture of CO and H_2 that plays a key role as the precursor for the synthesis of a range of energy-dense chemicals, including methanol, kerosene, and plastics.[2] Similarly, the nitrate reduction reaction (NO_3RR) offers an approach to close the NO_x cycle through conversion of waste nitrates/nitrogen oxides (such as those disposed of by various industries into local waterways or as exhaust) into NH_4^+ that may be further converted into ammonia, as a carbon-free energy carrier, as well as a fundamental chemical feedstock for the production of fertilizers.[3]

Recently, simultaneous CO_2RR and NO_3RR has also been employed to synthesize urea, the most commonly used N-based fertilizer, albeit the yields and selectivity of this pathway are

---

J. Leverett, J. A. Yuwono, P. Kumar, C. Kim, Q. Zhai, C. Han,
L. Dai, R. Daiyan, R. Amal
School of Chemical Engineering
UNSW Sydney
Sydney, NSW 2052, Australia
E-mail: r.daiyan@unsw.edu.au; r.amal@unsw.edu.au

T. Tran-Phu
Research School of Chemistry
The Australian National University
Canberra, ACT 2601, Australia

The ORCID identification number(s) for the author(s) of this article can be found under https://doi.org/10.1002/aenm.202201500.

DOI: 10.1002/aenm.202201500

J. A. Yuwono
College of Engineering and Computer Science
Australian National University
Canberra, ACT 2601, Australia

J. Qu, J. Cairney
Australian Centre for Microscopy and Microanalysis
The University of Sydney
Sydney, New South Wales 2006, Australia

A. N. Simonov
School of Chemistry and the ARC Centre of Excellence for
Electromaterials Science
Monash University
Melbourne, VIC 3800, Australia

R. K. Hocking
School of Science
Swinburne University of Technology
Melbourne, VIC 3122, Australia
E-mail: rhocking@swin.edu.au

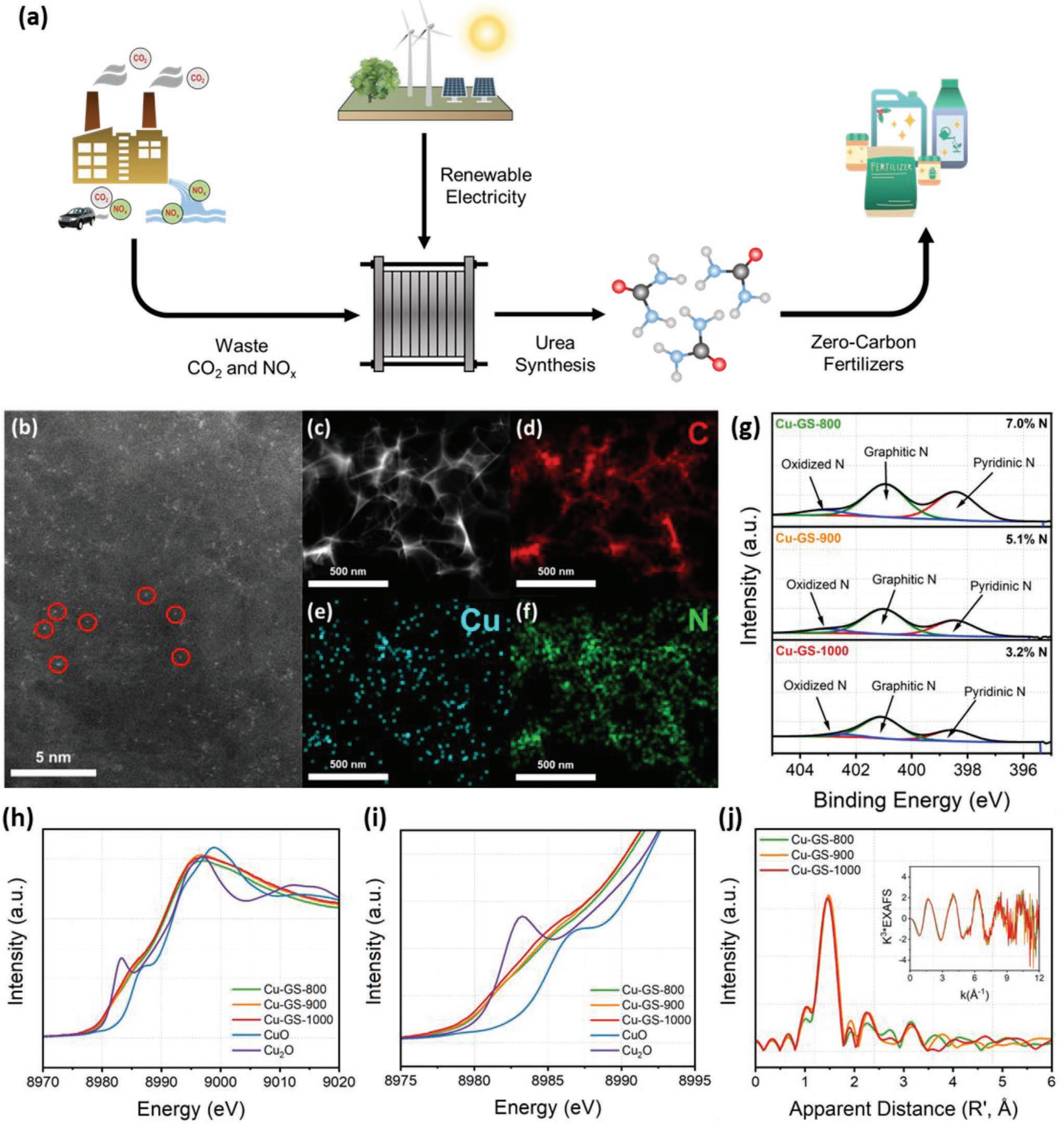

Figure 1. a) Schematic illustration for simultaneous CO_2RR and NO_3RR for net-zero carbon fertilizer production. b) HAADF-STEM imaging (some single atoms are circled in red). c–f) EDX mapping for as-synthesized Cu-GS-800. g) N 1s XPS fitting for as-synthesized Cu-GS-800, Cu-GS-900, and Cu-GS-1000. h–i) XANES spectra at Cu K-edge for as-synthesized Cu-GS-800, Cu-GS-900, and Cu-GS-1000, compared to reference $Cu^{II}O$ (Cu(II)) and Cu^{I}_2O (Cu(I)). j) Fourier transformed EXAFS at the Cu K-edge for Cu-GS-800, Cu-GS-900, and Cu-GS-1000.

low.[4] Compared to alternative nitrogenous fertilizers (such as ammonia), urea offers a higher N content, ease and safety of handling, and lower transportation costs.[5] The vast majority of urea (≈90%) is used as fertilizers (**Figure 1**a), with minor uses including the synthesis of plastics, resins, and adhesives as well as an agent in diesel engines to reduce emissions of nitric oxide.[6] Crucially, attaining high activity and selectivity toward urea production requires designing effective electrocatalysts with tunable active sites that assist in the adsorption of CO_2 and NO_x reactants, to facilitate the electrocatalytic coupling of C and N to form urea. Whilst a range of precious metal-based catalysts (including Ru, Pd, Au, and Ag) have been investigated for CO_2RR, NO_3RR, and urea production, the higher cost and scarcity of precious metals limit their application on a global scale.[7,8] As a more cost-effective transition metal, Cu has been found to exhibit activity for these energy conversion reactions.[9,10] For example, AuCu nanofibers,[11] Cu-doped TiO_2,[12] and metallic Cu[13] have been investigated for urea production; however, the individual electroreduction of CO_2 and NO_x strongly competes with the desired C-N coupling reaction required for a high selectivity of urea, leading to the generation of byproducts such as CO, HCOOH, and NH_4^+, and therefore a low selectivity for urea.

As focus shifts toward the synthesis of both cost-effective and highly active catalysts, carbon-based single atom catalysts (SACs) have gained recent attention for a range of energy conversion reactions, due to their low cost, minimal metal usage, and excellent activity facilitated by large surface areas and exposure of active sites.[14] Generally incorporating a transition metal single atom anchored to a carbon support through N doping, SACs have been employed for both the CO_2RR and, more recently, the NO_3RR. For example, Cu SACs exhibiting varying metal-nitrogen-carbon (M—N—C) moieties have been investigated for CO_2RR to a range of products, including CH_4,[15,16] $HCOO^-$,[17] CH_3OH,[18] and varying ratios of H_2 to CO.[19–23] As a high CO_2RR and NO_3RR activity are a prerequisite for the synthesis of urea, such SACs must exhibit strong binding of reaction intermediates to facilitate the electrochemical reduction of CO_2 and NO_3^- to urea. However, questions persist as to the role of the M—N—C coordination in dictating the activity and product selectivity for these reactions, such as the variation in the H_2:CO ratio seen with changing Cu—N—C coordination (from Cu-N_4 sites to Cu-N_3-C_1 and Cu-N_3-S_1 sites),[22,23] as well as the discrepancies in product selectivities noted between catalysts exhibiting Cu-N_4 sites, which have been reported as active for CO_2 reduction to CO, as well as to methanol, ethanol, and methane.[18,24,25] This is in direct contrast to reports for CO_2RR on catalysts exhibiting similar M—N—C moieties, such as Ni, which is consistently reported to convert CO_2 to CO at high selectivity on a range of Ni—N—C sites.[26,27] Conversely, there has been more limited application of Cu SACs for the NO_3RR.[28,29] For example, Cu atoms embedded in N-doped carbon nanosheets have been shown to reduce nitrate to NH_4^+ at high Faradaic efficiency compared to Cu nanoparticles (NPs) and bulk metal, through significant alleviation of nitrite production. Interestingly, density functional theory (DFT) calculations revealed that Cu-N_2 sites could be more favorable for nitrate adsorption when compared to Cu-N_4 sites, though not experimentally validated.[29]

Herein, we aim to provide a clear understanding of the correlation between the coordination environment of Cu single atoms within an N-doped carbon framework, and the activity toward the CO_2RR and NO_3RR energy conversion processes. These insights can assist in the development of highly active electrocatalysts for several conversion pathways, alleviating parallel research efforts into each field. Coordination tuning in SACs may provide new insights into the role that single atom coordination tuning plays in facilitating the coupling of C—N for urea synthesis, as demonstrated in the present study.

2. Results

The Cu SACs were synthesized according to our previously reported fabrication protocol (detailed in the Supporting Information).[27] Briefly, a solution consisting of a Cu salt, glucose, and dicyandiamide was combined with NaCl and lyophilized. The resulting powder was then annealed under Ar at various temperatures (800, 900, or 1000 °C), before the NaCl template and any remaining Cu nanoparticles were removed via acid washing. The powder was then annealed again under the same conditions, yielding Cu single atoms confined in graphene sheets; denoted Cu-GS-800, Cu-GS-900, and Cu-GS-1000 for the samples synthesized at 800, 900, and 1000 °C, respectively.

Structural characterization was first undertaken through scanning electron microscopy (SEM) imaging, revealing a similar macroporous framework structure for each catalyst (Figures S1 and S2, Supporting Information). This porous morphology is expected to provide large surface area for a maximized exposure of the active sites with an efficient mass transport.[30] At higher magnification, bright field transmission electron microscopy (TEM) imaging reveals the nanosheet structure of the graphene (Figure S3, Supporting Information). In addition, high angle annular dark-field scanning TEM (HAADF-STEM) suggests the absence of Cu nanoparticles and the presence of single atoms as bright spots throughout the carbon matrix (Figure 1b), which we attribute to the freeze-drying process that avoids aggregation of Cu into nanoparticles.[27] Energy dispersive X-ray (EDX) mapping (Figure 1c–f and Figures S4–S6, Supporting Information) shows a uniform dispersion of Cu and N throughout the carbon structure. This result agrees with the X-ray diffraction patterns (Figure S7, Supporting Information), from which we detect no peak for metallic Cu, confirming the absence of nanoparticles. The two broad diffraction peaks at $2\theta = 26°$ and 44° are assigned to the (002) and (101) planes of carbon, respectively.[31] Additionally, no peaks for NaCl are seen, concluding that the salt template is fully removed from the catalyst structure and therefore plays no role in the catalytic activity. Raman spectra (Figure S8, Supporting Information) exhibit the typical graphitic D (≈1350 cm^{-1}) and G (≈1600 cm^{-1}) bands, relating to defect carbon and sp^2-hybridized carbon, respectively.[32] The ratio of the D and G bands (I_D/I_G ratio) remains consistent (≈0.93) as the pyrolysis temperature is increased from 800 to 1000 °C, ruling out the possible role of carbon-based defects for either CO_2RR or NO_3RR.[33] The slight reduction in I_D/I_G from 0.94 to 0.92 indicates enhanced graphitization as the pyrolysis temperature increases, in agreement with previous reports.[34,35]

X-ray photoelectron spectroscopy (XPS) was carried out (Figure S9, Supporting Information) to probe the chemical composition and element states on the surface of the Cu-GS catalysts. Fitting of the N 1s spectra (Figure 1g) reveals the presence of oxidized N (≈403.2 eV), graphitic N (≈400.7 eV), and pyridinic N (≈398.2 eV) in each catalyst. Notably, as the pyrolysis temperature is increased from 800 to 1000 °C, the overall N content is reduced from 7.0 at% (Cu-GS-800) to 5.1 at% (Cu-GS-900), and finally to 3.2 at% (Cu-GS-1000). The largest decrease is noted for pyridinic N, which reduces from 3.0 at% in Cu-GS-800 to 1.0 at% in Cu-GS-1000. The high-resolution C 1s (Figure S10, Supporting Information) and O 1s (Figure S11, Supporting Information) spectra confirm the absence of Cu carbides or oxides in the catalysts, with peaks in the C 1s spectra representing graphite-like C—C (284.5 eV), C—N (285.9 eV), and C=O and O—C=O species (287.8 and 288.6 eV, respectively).[36,37] The Cu 2p spectra (Figure S12, Supporting Information) show that only one type of Cu species is present, the oxidation state of which inconsistent with tabulated Cu^0 and Cu^{2+} compounds.[38] A Cu surface concentration of ≈0.1 at% (0.5 wt%) was measured by XPS (Table S1, Supporting Information). However, inductively coupled plasma (ICP) optical emission spectroscopy measurements (Table S2, Supporting Information) reveal a Cu loading of ≈3–4 wt% for each catalyst, indicating that a significant proportion of the Cu is confined within the carbon structure.

To elucidate the coordination structure of Cu within the catalysts, we employed X-ray absorption spectroscopy (XAS) at the Cu K-edge. The X-ray absorption near-edge structure (XANES) spectra of the catalysts (Figure 1h,i) are similar to each other and to other compounds with a similar $Cu\text{-}N_4$ coordination, with energies between the Cu(I) and Cu(II) reference spectra.[39,40] There is no pre-edge above background present in the data, which is usually consistent with Cu(I) and a $3d^{10}$ electron configuration. However, as the Cu-GS catalysts can contain a combination of structurally different sites, this may have the effect of cancelling out the pre-edge features.[41] There is a slight energy difference in the XANES of the materials consistent with a shift to lower effective nuclear charge with higher annealing temperature. The Cu K-edge extended X-ray absorption fine edge structure (EXAFS) spectra (Figure 1j) are close to featureless and are well accounted for by four Cu–N interactions. A second coordination sphere is above error at the apparent distance (R') of 2.1 Å (detailed in the Supporting Information) and can be accounted for by additional Cu—C interactions expected in this matrix, as the annealing temperature is increased.

Further, the catalysts were investigated by cyclic voltammetry to compare their electrochemically active surface area (ECSA). Regardless the pyrolysis temperature, the ECSA was ≈125 cm^2_{ECSA} per $cm^2_{GEOMETRIC}$ (Figure S13, Supporting Information), from which we infer (with a comparable Cu loading determined above for each catalyst) that the number of active sites accessible to the reactants is also similar for these materials. Through fitting an equivalent circuit to electrochemical impedance spectroscopy measurements at potential where no significant Faradic processes occur (Figure S14, Supporting Information), we observe a low and comparable resistance for charge transfer within each of the catalysts, indicating a similar conductivity between the Cu-GS-800, Cu-GS-900, and Cu-GS-1000 electrodes.

Collectively, these physical and electrochemical characterization results highlight the similar structure for each of the Cu-GS catalysts, consisting of Cu single atoms coordinated with N and/or C within the 3D amorphous graphene matrix. As such, we propose that any unique activity for the CO_2RR and NO_3RR achieved with each catalyst is a direct result of the slight variation in Cu coordination structure, as some $Cu\text{-}N_4$ sites are converted to $Cu\text{-}N_{4-x}\text{-}C_x$ sites as the pyrolysis temperature is increased from 800 to 1000 °C, which is consistent with the XAS measurements.

The CO_2RR activity of the catalysts was first tested in a two compartment H-cell system. The Faradaic efficiency for CO (FE_{CO}) notably reduces (**Figure 2**a) with increasing pyrolysis

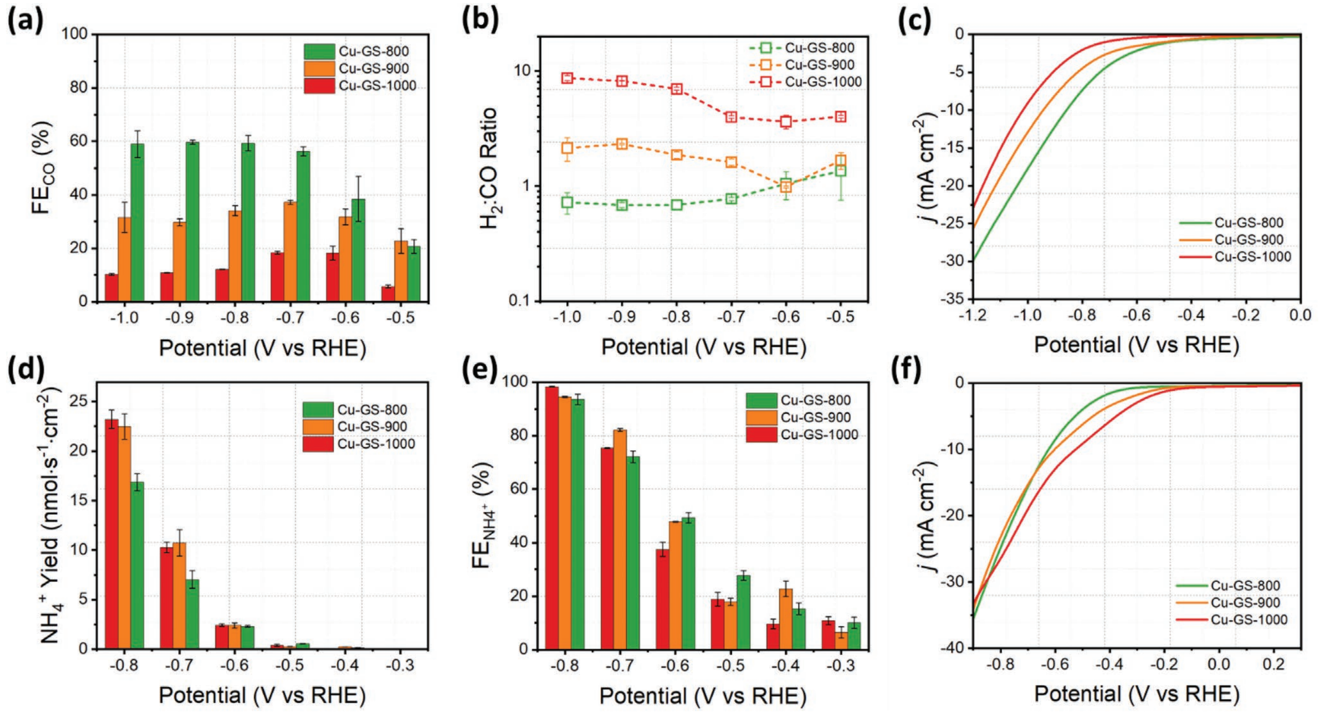

Figure 2. Electrocatalytic CO_2RR and NO_3RR performance. Dependence of a) the Faradaic efficiency for CO and b) the syngas ratio on applied potential, for Cu-GS-800, Cu-GS-900, and Cu-GS-1000. c) CO_2RR polarization curves (scan rate: 5 mV s^{-1}) in CO_2-saturated 0.1 м $KHCO_3$. Dependence of d) the NH_4^+ yield rate and e) the Faradaic efficiency of NH_4^+ on applied potential, for Cu-GS-800, Cu-GS-900, and Cu-GS-1000. f) NO_3RR polarization curves (scan rate: 5 mV s^{-1}) in Ar-saturated 0.1 м K_2SO_4 + 0.1 м KNO_3.

temperature. For example, at –0.8 V versus the reversible hydrogen electrode (RHE), the FE_{CO} values were 59%, 34%, and 12% for Cu-GS-800, Cu-GS-900, and Cu-GS-1000, respectively. In contrast, the FE_{H2} (Figure S15, Supporting Information) follows the trend Cu-GS-1000 > Cu-GS-900 > Cu-GS-800, with each catalyst achieving an FE_{H2} of 85%, 63%, and 40%, at –0.8 V versus RHE, respectively. This result is in agreement with some studies on Cu SACs for CO_2RR, which report high FE_{CO} values of ≈80–90% at –1.0 V versus RHE on Cu-N_4 sites,[19,20] whilst an undercoordinated (or unsaturated) Cu-N_3-C_1 achieved an FE_{CO} of ≈20% at the same potential.[23] Interestingly, the hydrogen evolution reaction (HER) activity in Ar-saturated 0.1 м $KHCO_3$ (Figure S16, Supporting Information) is comparable between each catalyst (in agreement with our HER results in acidic and alkaline environments, Figure S17, Supporting Information). This indicates that the HER activity remains consistent as the pyrolysis temperature is varied across the catalysts and that the change in activity is associated with the fact that Cu-N_4 sites catalyze the reduction of CO_2 to CO. This variation in activity is further highlighted by the H_2:CO ratio achieved with each catalyst (Figure 2b). Whilst the Cu-GS-800 catalyst maintains a consistent syngas ratio of ≈0.7 across most of the potential range tested, the H_2:CO ratio slowly increased (from 1.0 to 2.3 and from 3.6 to 8.7 on Cu-GS-900 and Cu-GS-1000, respectively) as the applied potential is changed from –0.6 to –1.0 V versus RHE. In fact, the syngas ratios achieved on Cu-GS-800 and Cu-GS-900 lie in the ranges useful for the chemical manufacturing industry, such as for the Fischer-Tropsch synthesis of olefins and kerosene.[42] Long-term stability testing with the Cu-GS-800 catalyst shows a stable current density (*j*) of –17 mA cm^{-2} and an FE_{CO} of ≈60% at –1.0 V versus RHE over a 12 h period (Figure S18, Supporting Information).

From the polarization curves (Figure 2c), we note that increasing the pyrolysis temperature leads to a decrease in *j*, with Cu-GS-800, Cu-GS-900, and Cu-GS-1000 attaining a *j* of –18, –13, and –9 mA cm^{-2} at –1.0 V versus RHE (comparable to benchmarked Cu SACs for CO_2RR, Table S3, Supporting Information). We infer that this difference results from the significantly higher intrinsic activity for CO_2RR on the Cu-N_4 sites (Cu-GS-800) compared to the Cu-N_{4-x}-C_x sites. Nuclear magnetic resonance (NMR) analysis reveals no liquid products, with a negligible Faradaic efficiency for ethanol, which is less than 0.1% at each potential with each catalyst (Table S4, Supporting Information) and may be formed on remaining Cu NPs or nanoclusters (which were however not detected through our extensive TEM imaging, XPS, or XAS analysis) or from impurities introduced during NMR measurements. We therefore propose that such Cu—N—C atomic sites are active for CO_2RR to CO, rather than to more thermodynamically complex reduction products (such as methanol, formic acid, or the range of products that Cu is known to generate), to which the CO_2RR is unfavorable due to the high energy barrier associated with a greater than two-electron CO_2 reduction process on single atom sites.[15] However, it has also been found that Cu—N—C sites can be reversibly converted to small Cu NPs in situ during CO_2RR, which explains the potential presence of products such as methane, methanol, and ethanol on Cu catalysts in literature.[24,25] We do not see a significant yield of such products, and therefore propose that this process does not occur with the Cu-GS catalysts. A better understanding of i) the factors that influence whether this conversion to Cu NPs will occur in a specific catalyst and ii) the active sites that are created in situ during this process, can promote the investigation of Cu SACs for tuning CO_2RR to a vast range of products and product selectivities.

We then investigated the NO_3RR performance of each catalyst. Whilst it has been shown that the NH_4^+ yield rate can be improved in an alkaline environment as the NO_3RR kinetics increase[43,44] (elaborated in Figure S19, Supporting Information), we employ an Ar-saturated 0.1 м K_2SO_4 + 0.1 м KNO_3 solution to suppress the HER, in order to effectively gauge the influence of Cu—N—C coordination on the NO_3RR activity. Ar saturation is required to avoid the interference of the nitrogen reduction reaction and the oxygen reduction reaction, for both of which Cu SACs have been found to be active, and as such their possible contribution cannot be ignored (Figure S20, Supporting Information).[45–47] A comparison of the polarization curves (Figure 2f) and without the addition of KNO_3 (Figure S21, Supporting Information) confirms that the activity is arising from NO_3RR. It is also evident from the polarization curves that each catalyst exhibits a similar *j* at –0.8 V versus RHE, of –25, –23, and –27 mA cm^{-2} on Cu-GS-800, Cu-GS-900, and Cu-GS-1000, respectively.

We note (Figure 2d) that the NH_4^+ yield rate is quite consistent between each catalyst from –0.3 to –0.7 V versus RHE; however, yield rates of 23, 22, and 17 nmol s^{-1} cm^{-2} (corresponding to 2200, 2900, and 3000 µg h^{-1} mg_{cat}^{-1}) are attained at –0.8 V versus RHE on Cu-GS-800, Cu-GS-900, and Cu-GS-1000, respectively. In fact, a previous DFT study has found that the calculated adsorption energy for NO_3^- is lower on Cu-N_2 sites compared to Cu-N_4, and as such, that the Cu-N_{4-x}-C_x sites may be more favorable for the NO_3RR.[29] Nevertheless, the Faradaic efficiency for ammonium (FE_{NH4^+}) remains consistent with each catalyst across the potential range tested (Figure 2e), with a maximum FE_{NH4^+} of 94%, 95%, and 98% achieved at –0.8 V versus RHE with Cu-GS-800, Cu-GS-900, and Cu-GS-1000, respectively (Figure 2e), indicating that the Cu-N_{4-x}-C_x sites exhibit a slightly higher activity and selectivity toward ammonium production at this potential. This FE_{NH4^+} value is amongst the highest recorded for SACs employed for NO_3RR (Table S5, Supporting Information) and remains stable over an extended period of 12 h (Figure S22, Supporting Information). A higher FE_{NH4^+} is seen at more negative potentials, likely due to more complete conversion of the intermediate NO_2^- to NH_4^+.[43] The high FE_{NH4^+} achieved at more negative potentials with each catalyst aligns with reports that nitrite production is significantly alleviated on Cu atomic sites compared to metallic Cu catalysts, due to the higher adsorption of NO_2^- on Cu—N—C sites.[29] FE_{H2} is effectively suppressed (Figure S23, Supporting Information), with no H_2 peaks visible in the thermal conductivity detection in gas chromatography measurements (Figure S24, Supporting Information) until –0.7 V versus RHE, and FE_{H2} remains ≤ 1% for all catalysts at –0.8 V versus RHE.

To gain further insights into the CO_2RR and NO_3RR activity on various Cu—N—C coordination structures, we carry out DFT calculations for the energy changes involved with each reaction pathway (Figure S25, Supporting Information). There is some debate in terms of the rate-determining step (RDS) for

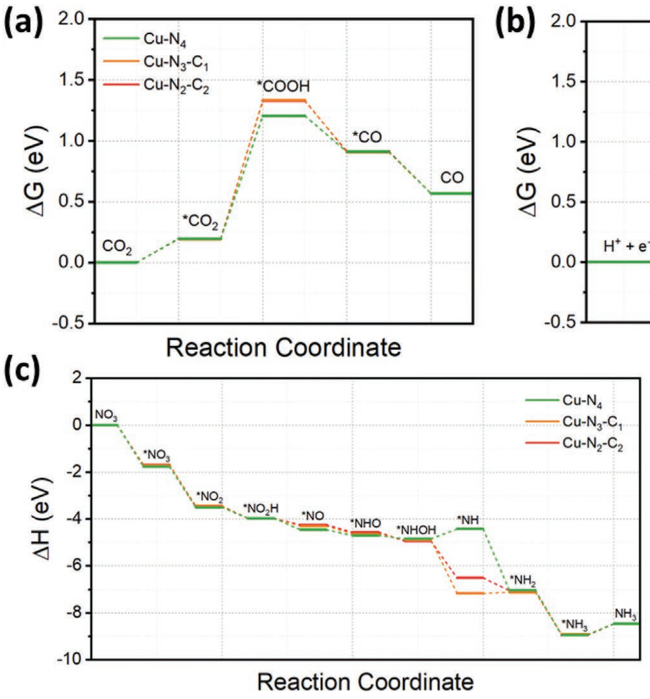

Figure 3. Reaction pathways for a) CO_2RR to CO, b) HER in an acidic medium, and c) NO_3RR to NH_3. d) Graphical representations of modeled Cu—N—C sites.

the CO_2RR. It has been reported that the first elementary step (the adsorption of CO_2 to the catalyst surface, $CO_2 + * + e^- \rightarrow *CO_2^-$) is the RDS,[48] whilst contradictory DFT calculations and quantum calculations have proposed that the transfer of protons to *CO_2^- to form *COOH is the RDS for metal single atom sites.[49,50] We note (**Figure 3**a) that the energy change associated with the first elementary step is similar between each modeled site, whilst the formation of *COOH is more favorable on Cu-N_4, compared to Cu-N_3-C_1 and Cu-N_2-C_2, with a Gibbs free energy (ΔG) of 1.21, 1.33, and 1.33 eV, respectively. As such, we propose that this is the RDS for CO_2RR on the Cu-GS catalysts, and therefore the Cu-GS-800 catalyst (exhibiting Cu-N_4 sites) should achieve a higher catalytic performance for CO_2RR (in agreement with our experimental results, Figure 2a). We also investigated the competing HER (that accompanies both CO_2RR and NO_3RR) through the *H reaction step, the key intermediate in this reaction.[49] We find that the ΔG for *H adsorption (Figure 3b) is similar for each catalyst (1.34, 1.38, and 1.32 eV on Cu-N_4, Cu-N_3-C_1, and Cu-N_2-C_2 sites, respectively), which may explain the similar HER activity of each catalyst in acidic, alkaline, and neutral environments (Figures S16 and S17, Supporting Information). It is therefore expected that the HER performance is similar between each catalyst, and thus the CO_2RR activity is dictated by formation of the *COOH intermediate (which is more energetically favorable on Cu-N_4 sites, compared to Cu-N_{4-x}-C_x sites).

Subsequently, we explore the various NO_3RR reaction pathways that result in the formation of NH_3 (Figure 3c and Figure S26, Supporting Information). Several steps have been proposed as the RDS on single atoms sites for NO_3RR, including the first step of NO_3^- adsorption, *NO reduction to *NHO, and *NHO reduction to *N.[22,41] However, we find that the reaction pathways exhibit similar energies on each site, which is reflected in our experimental results, where a comparable FE_{NH4^+} is achieved with each catalyst across the potential range tested. We note that in one modeled pathway (Figure 3c), a significant difference is seen in the energy for *NH formation on the Cu-N_4 sites (Figure 3c), of –4.43 eV (leading to an uphill process) compared to –7.17 eV and –6.51 eV on Cu-N_3-C_1 and Cu-N_2-C_2 sites, respectively. This may be a potential rate limiting step in the NO_3RR, and could explain the slight increase in FE_{NH4^+} at more negative potentials (i.e., at –0.8 V vs RHE) as the pyrolysis temperature is increased from 800 to 1000 °C (causing the conversion of some Cu-N_4 sites to Cu-N_{4-x}-C_x sites).

Finally, we explored simultaneous CO_2RR and NO_3RR. In order to generate urea from concurrent CO_2RR and NO_3RR, the ability of a catalyst to adsorb both CO_2 and NO_3^- reactants is required for C—N coupling.[4] Metal-based catalysts that have been investigated for urea production have exhibited activity for CO_2RR to CO, indicating that a high CO_2 reduction capability is imperative for synthesizing urea.[11,51,52] On the basis of the above experimental results and DFT calculations, it is clear that the Cu-GS catalysts exhibit catalytic activity for these reactions and therefore present the potential for catalyzing CO_2 and NO_3^- to urea. We test this hypothesis through carrying out both CO_2RR and NO_3RR. When tested for urea production, interestingly, the FE_{CO} reduces close to zero with Cu-GS-800 at more negative potentials (**Figure 4**a), to which we attribute the enhanced coupling of *CO_2 and *NO_2 for an increased urea yield rate on Cu-GS-800. This provides the first indication that the Cu-GS-800 catalyst may be more active for urea production, due to its greater CO_2RR capability compared to Cu-GS-900 and Cu-GS-1000. Indeed, at –1.0 V versus RHE, the

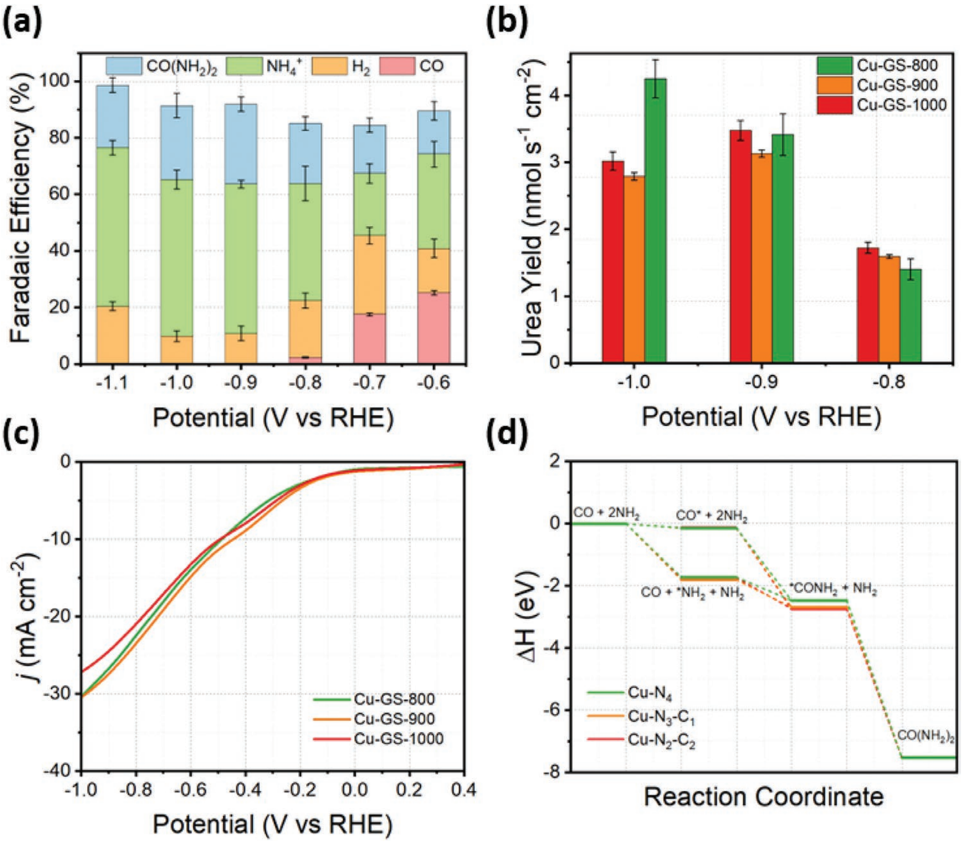

Figure 4. a) Dependence of the Faradaic efficiencies on applied potential in the H-cell system with Cu-GS-800. b) Urea yield rate and c) polarization curves for Cu-GS-800, Cu-GS-900, and Cu-GS-1000. d) Reaction pathway for urea production from simultaneous CO_2RR and NO_3RR.

urea yield rate is 4.3 nmol s^{-1} cm^{-2} (1800 µg h^{-1} mg_{cat}^{-1}) with Cu-GS-800, compared to 2.8 and 3.0 nmol s^{-1} cm^{-2} (1200 and 1300 µg h^{-1} mg_{cat}^{-1}) with Cu-GS-900 and Cu-GS-1000, respectively (Figure 4b). We find that the maximum FE_{urea} of 28% is achieved with Cu-GS-800 at –0.9 V versus RHE, whilst Cu-GS-900 and Cu-GS-1000 achieve an FE_{urea} of 25% and 23% at the same potential, respectively (Figure S27, Supporting Information). A similar *j* is achieved for each of the catalysts (Figure 4c). As indicated by the lack of CO_2RR and NO_3RR activity in electrolytes without CO_2 saturation (Figure S16, Supporting Information), or NO_3^- presence (Figure S21, Supporting Information), respectively, the urea is produced through reduction of the CO_2 gas and NO_3^-. In order to further exclude the C present in each catalyst as a source for urea production (as each Cu-GS catalyst consists of ≈90 at% C), we undertook isotope labeling experiments, saturating the electrolyte with $^{13}CO_2$. The ^{13}C NMR spectra (Figure S28, Supporting Information) displays a prominent peak at ≈162 ppm, confirming the formation of urea as a result of $^{13}CO_2$ reduction.[4,53] Further, to exclude the role of N in the catalyst in both NH_4^+ and urea production, we determine (detailed in the Supporting Information), that the N present in the produced NH_4^+ through one bulk electrolysis is over an order of magnitude greater than the N content in the Cu-GS-800 catalyst, confirming the reduction of NO_3^- for both NO_3RR and urea production. The presence of Cu ions in the electrolyte solutions following CO_2RR, NO_3RR, and urea production was also determined through ICP measurements (Table S6, Supporting Information). The low concentration indicates that the presence of NO_3^- and NH_4^+ does not further corrode the Cu in the single atom catalysts, in agreement with reports in literature.[29] To the best of our knowledge, we herein report the first published study of single atom catalyst for urea production from simultaneous CO_2RR and NO_3RR. The activity of the Cu-GS-800 catalyst is comparable to metal-based catalysts explored in the few studies on electrochemical urea production from CO_2 and NO_x (Table S7, Supporting Information).

DFT calculations undertaken for one possible reaction pathway (Figure 4d) reveal that the energy barriers for the C—N bond formation (required to produce urea) from *CO and *NH_2 are comparable on each of the modeled sites, with a slightly more favorable energy associated with this step on Cu-N_3-C_1 (2.69 eV) and Cu-N_2-C_2 sites (2.74 eV), compared to Cu-N_4 (2.47 eV). As such, it is conceivable that the energy changes associated with the *CO and *NH_2 formation could be a potential descriptor for catalytic activity toward the urea production.[52] We note that the Cu-GS-800 catalyst is the most active for both CO_2RR and urea synthesis, and we therefore propose that the CO formation is the RDS in aqueous environment, as the comparably lower concentration of CO_2 competes with NO_3^- at active sites.[4] This has been shown in the literature, where increasing the NO_x concentration leads to enhanced NH_3 production whilst the FE_{CO} and FE_{urea} significantly decrease.[52] As the *NO_2 and *CO_2 intermediates should be coupled at an early stage of the reaction (to achieve an increased urea selectivity rather than byproducts such as NH_3, CO, or HCOOH),[4] it is reasonable that the formation of the *COOH intermediate is an RDS for both CO_2RR and urea production. This is in agreement with our DFT calculations, which reveal that CO_2RR is more favorable on Cu-N_4 sites.

3. Conclusion

In summary, we have investigated the role that Cu—N—C coordination plays for both the CO_2RR and NO_3RR. XAS measurements are consistent with the synthesized Cu SACs exhibiting a change from Cu-N_4 sites to Cu-N_{4-x}-C_x sites, as the pyrolysis temperature is increased from 800 to 1000 °C. This change in the coordination sphere leads to variation in their catalytic activity, with the Cu-N_4 sites exhibiting a higher activity toward CO_2RR, whilst Cu-N_{4-x}-C_x sites achieve a greater NH_4^+ yield rate during NO_3RR (in agreement with our DFT calculations). We then coupled the CO_2RR and NO_3RR, achieving a Faradaic efficiency of 28% for urea on Cu-N_4 sites, with a production rate of 4.3 nmol s^{-1} cm^{-2} at −0.9 V versus RHE attained with the Cu-GS-800 catalyst. To the best of our knowledge, this is the first report for the urea production with single atom catalysts. This result demonstrates the potential for the conversion of renewable energy to net-zero fertilizers via electrochemical urea synthesis on highly active single atom catalysts.

Supporting Information

Supporting Information is available from the Wiley Online Library or from the author.

Acknowledgements

All material and surface characterizations were carried out at the Mark Wainwright Analytical Centre (MWAC), UNSW. The work was supported by the Australian Research Council (ARC) Research Hub on Integrated Energy Storage Solutions (IH180100020) and ARC Training Centre for The Global Hydrogen Economy (IC200100023). The authors acknowledge the technical and scientific support of the Microscopy Australia node at UNSW (Electron Microscope Unit) and the University of Sydney. The authors also acknowledge the assistance of resources and services from the National Computational Infrastructure (NCI), which was supported by the Australian Government.

Open access publishing facilitated by University of New South Wales, as part of the Wiley - University of New South Wales agreement via the Council of Australian University Librarians.

Conflict of Interest

The authors declare no conflict of interest.

Author Contributions

R.D. and R.A. conceived the idea and directed the research. J.L. carried out material synthesis, characterization, and activity testing. R.K.H. and T.T.-P. carried out synchrotron measurements and analysis. J.Q. and J.C. carried out TEM imaging and associated measurements. C.K. and Q.Z. carried out urea quantification. P.K. and J.A.Y. carried out density functional theory calculations. J.L., R.D., J.A.Y., P.K., R.K.H., and R.A. cowrote the paper. All authors contributed to analyzing results and discussion.

Data Availability Statement

The data that support the findings of this study are available in the supplementary material of this article.

Keywords

CO_2 reduction, Cu single atom, power to X, urea

Received: May 1, 2022
Revised: June 8, 2022

---

[1] R. Daiyan, I. Macgill, R. Amal, *ACS Energy Lett.* **2020**, *5*, 3843.
[2] S. R. Foit, I. C. Vinke, L. G. J. de Haart, R. A. Eichel, *Angew. Chem., Int. Ed.* **2017**, *56*, 5402.
[3] Y. Zeng, C. Priest, G. Wang, G. Wu, *Small Methods* **2020**, *4*, 2000672.
[4] C. Lv, L. Zhong, H. Liu, Z. Fang, C. Yan, M. Chen, Y. Kong, C. Lee, D. Liu, S. Li, J. Liu, L. Song, G. Chen, Q. Yan, G. Yu, *Nat. Sustainable* **2021**, *4*, 868.
[5] M. Xia, C. Mao, A. Gu, A. A. Tountas, C. Qiu, T. E. Wood, Y. F. Li, U. Ulmer, Y. Xu, C. J. Viasus, J. Ye, C. Qian, G. Ozin, *Angew. Chem., Int. Ed.* **2022**, *61*, e202110158.
[6] J. H. Baik, S. D. Yim, I. S. Nam, Y. S. Mok, J. H. Lee, B. K. Cho, S. H Oh, *Top. Catal.* **2004**, *30*, 37.
[7] D. Friedman, T. Masciangioli, S. Olson, in *The Role of the Chemical Sciences in Finding Alternatives to Critical Resources*, National Academies Press, Washington (DC), USA **2012**, pp. 21–28.
[8] J. Li, G. Zhan, J. Yang, F. Quan, C. Mao, Y. Liu, B. Wang, F. Lei, L. Li, A. W. M. Chan, L. Xu, Y. Shi, Y. Du, W. Hao, P. K. Wong, J. Wang, S. X. Dou, L. Zhang, J. C. Yu, *J. Am. Chem. Soc.* **2020**, *142*, 7036.
[9] X. Fu, X. Zhao, X. Hu, K. He, Y. Yu, T. Li, Q. Tu, X. Qian, Q. Yue, M. R. Wasielewski, Y. Kang, *Appl. Mater. Today* **2020**, *19*, 100620.
[10] Y. Wang, A. Xu, Z. Wang, L. Huang, J. Li, F. Li, J. Wicks, M. Luo, D. H. Nam, C. S. Tan, Y. Ding, J. Wu, Y. Lum, C. T. Dinh, D. Sinton, G. Zheng, E. H. Sargent, *J. Am. Chem. Soc.* **2020**, *142*, 5702.
[11] S. Liu, S. Yin, Z. Wang, Y. Xu, X. Li, L. Wang, H. Wang, *Cell Rep. Phys. Sci.* **2022**, *3*, 100869.
[12] N. Cao, Y. Quan, A. Guan, C. Yang, Y. Ji, L. Zhang, G. Zheng, *J. Colloid Interface Sci.* **2020**, *577*, 109.
[13] D. Aurbach, A. Zaban, A. Schechter, Y. Em-Eli, E. Zin-igrad, B. Markovsky, I. Yoshimatsu, T. Hirai, J. Yamaki, J. Electrochem, K. Saito, M. Arakawa, S. Tobishima, D. Kagaku, J. Dahn, A. Sleigh, H. Shi, B. Way, W. Weydanz, J. N. Reimer, Q. Zhong, U. von Sacken, I. Li, W. Gorecki, R. Andreani, C. Berthier, M. B. Armand, M. Mali, D. Brinkmann, K. Nagaoka, et al., *ECS* **1998**, *145*, 659.
[14] Y. Wang, X. Zheng, D. Wang, *Nano Res.* **2022**, *15*, 1730.
[15] Y. Cai, J. Fu, Y. Zhou, Y. C. Chang, Q. Min, J. J. Zhu, Y. Lin, W. Zhu, *Nat. Commun.* **2021**, *12*, 586.
[16] S. Chen, W. H. Li, W. Jiang, J. Yang, J. Zhu, L. Wang, H. Ou, Z. Zhuang, M. Chen, X. Sun, D. Wang, Y. Li, *Angew. Chem., Int. Ed.* **2022**, *61*, 202114450.
[17] C. Cometto, A. Ugolotti, E. Grazietti, A. Moretto, G. Bottaro, L. Armelao, C. di Valentin, L. Calvillo, G. Granozzi, *npj 2D Mater. Appl.* **2021**, *5*, 63.

[18] H. Yang, Y. Wu, G. Li, Q. Lin, Q. Hu, Q. Zhang, J. Liu, C. He, *J. Am. Chem. Soc.* **2019**, *141*, 12717.
[19] H. Cheng, X. Wu, X. Li, X. Nie, S. Fan, M. Feng, Z. Fan, M. Tan, Y. Chen, G. He, *Chem. Eng. J.* **2020**, *407*, 126842.
[20] C. Xu, X. Zhi, A. Vasileff, D. Wang, B. Jin, Y. Jiao, Y. Zheng, S.-Z. Qiao, *Small Struct.* **2021**, *2*, 2000058.
[21] L. Yan, X. du Liang, Y. Sun, L. P. Xiao, B. A. Lu, G. Li, Y. Y. Li, Y. H. Hong, L. Y. Wan, C. Chen, J. Yang, Z. Y. Zhou, N. Tian, S. G. Sun, *Chem. Commun.* **2022**, *58*, 2488.
[22] D. Chen, L. H. Zhang, J. Du, H. Wang, J. Guo, J. Zhan, F. Li, F. Yu, *Angew. Chem., Int. Ed.* **2021**, *60*, 24022.
[23] Z. Luo, Z. Yin, J. Yu, Y. Yan, B. Hu, R. Nie, A. F. Kolln, X. Wu, R. K. Behera, M. Chen, L. Zhou, F. Liu, B. Wang, W. Huang, S. Zhang, L. Qi, *Small* **2022**, *18*, 2107799.
[24] Z. Weng, Y. Wu, M. Wang, J. Jiang, K. Yang, S. Huo, X. F. Wang, Q. Ma, G. W. Brudvig, V. S. Batista, Y. Liang, Z. Feng, H. Wang, *Nat. Commun.* **2018**, *9*, 415.
[25] D. Karapinar, N. T. Huan, N. R. Sahraie, J. Li, D. Wakerley, N. Touati, S. Zanna, D. Taverna, L. H. G. Tizei, A. Zitolo, F. Jaouen, V. Mougel, M. Fontecave, *Angew. Chem., Int. Ed.* **2019**, *58*, 15098.
[26] X. Li, W. Bi, M. Chen, Y. Sun, H. Ju, W. Yan, J. Zhu, X. Wu, W. Chu, C. Wu, Y. Xie, *J. Am. Chem. Soc.* **2017**, *139*, 14889.
[27] J. Leverett, J. A. Yuwono, P. Kumar, T. Tran-Phu, J. Qu, J. Cairney, X. Wang, A. N. Simonov, R. K. Hocking, B. Johannessen, L. Dai, R. Daiyan, R. Amal, *ACS Energy Lett.* **2022**, *7*, 920.
[28] X. Zhao, X. Jia, Y. He, H. Zhang, X. Zhou, H. Zhang, S. Zhang, Y. Dong, X. Hu, A. v. Kuklin, G. v. Baryshnikov, H. Ågren, G. Hu, *Appl. Mater. Today* **2021**, *25*, 101206.
[29] T. Zhu, Q. Chen, P. Liao, W. Duan, S. Liang, Z. Yan, C. Feng, *Small* **2020**, *16*, 2004526.
[30] Y. Li, Z. S. Wu, P. Lu, X. Wang, W. Liu, J. Ma, W. Ren, Z. Jiang, X. Bao, *Adv. Sci.* **2020**, *7*, 1903089.
[31] M. S. Seehra, V. Narang, U. K. Geddam, A. B. Stefaniak, *Carbon* **2017**, *111*, 380.
[32] A. C. Ferrari, D. M. Basko, *Nat. Nanotechnol.* **2013**, *8*, 235.
[33] M. S. Dresselhaus, A. Jorio, A. G. Souza Filho, R. Saito, *Philos. Trans. R. Soc., A:* **2010**, *368*, 5355.
[34] H. Cheng, X. Wu, X. Li, X. Nie, S. Fan, M. Feng, Z. Fan, M. Tan, Y. Chen, G. He, *Chem. Eng. J.* **2020**, *407*, 126842.
[35] R. Daiyan, X. Zhu, Z. Tong, L. Gong, A. Razmjou, R.-S. Liu, Z. Xia, X. Lu, L. Dai, R. Amal, *Nano Energy* **2020**, *78*, 105213.
[36] D. J. Morgan, *C (Basel)* **2021**, *7*, 51.
[37] M. Ayiania, M. Smith, A. J. R. Hensley, L. Scudiero, J. S. McEwen, M. Garcia-Perez, *Carbon* **2020**, *162*, 528.
[38] M. C. Biesinger, *Surf. Interface Anal.* **2017**, *49*, 1325.
[39] N. C. Tomson, K. D. Williams, X. Dai, S. Sproules, S. Debeer, T. H. Warren, K. Wieghardt, *Chem. Sci.* **2015**, *6*, 2474.
[40] J. Chaboy, A. Muñoz-Páez, F. Carrera, P. Merkling, E. S. Marcos, *Phys. Rev. B: Condens. Matter Mater. Phys.* **2005**, *71*, 134208.
[41] B. v. Kerr, H. J. King, C. F. Garibello, P. R. Dissanayake, A. N. Simonov, B. Johannessen, D. S. Eldridge, R. K. Hocking, *Energy Fuels* **2022**, *36*, 2369.
[42] I. Wender, *Annu. Rev. Energy* **1986**, *11*, 295.
[43] Z. Y. Wu, M. Karamad, X. Yong, Q. Huang, D. A. Cullen, P. Zhu, C. Xia, Q. Xiao, M. Shakouri, F. Y. Chen, J. Y.(Timothy) Kim, Y. Xia, K. Heck, Y. Hu, M. S. Wong, Q. Li, I. Gates, S. Siahrostami, H. Wang, *Nat. Commun.* **2021**, *12*, 2870.
[44] R. Chauhan, V. C. Srivastava, *Chem. Eng. Sci.* **2022**, *247*, 117025.
[45] W. Zang, T. Yang, H. Zou, S. Xi, H. Zhang, X. Liu, Z. Kou, Y. Du, Y. P. Feng, L. Shen, L. Duan, J. Wang, S. J. Pennycook, *ACS Catal.* **2019**, *9*, 10166.
[46] L. Cui, L. Cui, Z. Li, J. Zhang, H. Wang, S. Lu, Y. A. Xiang, *J. Mater. Chem. A* **2019**, *7*, 16690.
[47] F. Li, G.-F. Han, H.-J. Noh, S.-J. Kim, Y. Lu, B. Hu, Y. Jeong, Z. Fu, J.-B. Baek, *Energy Environ. Sci.* **2018**, *11*, 2263.
[48] W. Deng, P. Zhang, B. Seger, J. Gong, *Nat. Commun.* **2022**, *13*, 803.
[49] M. D. Hossain, Y. Huang, T. H. Yu, W. A. Goddard, Z. Luo, *Nat. Commun.* **2020**, *11*, 2256.
[50] M. R. Singh, J. D. Goodpaster, A. Z. Weber, M. Head-Gordon, A. T. Bell, *PNAS* **2017**, *114*, E8812.
[51] M. Yuan, J. Chen, Y. Bai, Z. Liu, J. Zhang, T. Zhao, Q. Wang, S. Li, H. He, G. Zhang, *Angew. Chem., Int. Ed.* **2021**, *60*, 10910.
[52] Y. Feng, H. Yang, Y. Zhang, X. Huang, L. Li, T. Cheng, Q. Shao, *Nano Lett.* **2020**, *20*, 8282.
[53] O. Steinhof, É. J. Kibrik, G. Scherr, H. Hasse, *Magn. Reson. Chem.* **2014**, *52*, 138